CHEMISTRY

Highly active dry methane reforming catalysts with boosted in situ grown Ni-Fe nanoparticles on perovskite via atomic layer deposition

Sangwook Joo[1]*, Arim Seong[1]*, Ohhun Kwon[1], Kyeounghak Kim[2], Jong Hoon Lee[3], Raymond J. Gorte[4], John M. Vohs[4†], Jeong Woo Han[2†], Guntae Kim[1†]

With the need for more stable and active metal catalysts for dry reforming of methane, in situ grown nanoparticles using exsolution are a promising approach. However, in conventional exsolution, most nanoparticles remain underneath the surface because of the sluggish diffusion rate of cations. Here, we report the atomic layer deposition (ALD)–combined topotactic exsolution on $La_{0.6}Sr_{0.2}Ti_{0.85}Ni_{0.15}O_{3-\delta}$ toward developing active and durable catalysts. The uniform and quantitatively controlled layer of Fe via ALD facilitates the topotactic exsolution, increasing finely dispersed nanoparticles. The introduction of Fe_2O_3 yields the formation of Ni-Fe alloy owing to the spontaneous alloy formation energy of −0.43 eV, leading to an enhancement of the catalytic activity for dry methane reforming with a prolonged stability of 410 hours. Overall, the abundant alloy nanocatalysts via ALD mark an important step forward in the evolution of exsolution and its application to the field of energy utilization.

INTRODUCTION

Supported metal catalysts have been extensively used in the fields of catalysis, energy conversion, and energy storage [e.g., dry reforming of methane (DRM)], but catalyst deactivation due to agglomeration or coking restrains the catalyst lifetime and efficiency (*1*–*3*). The exsolution of metal nanoparticles from the host oxide lattice to the surface has been the subject of extensive studies to overcome these difficulties (*4*–*7*). The exsolution, called in situ growth, offers solid and stable nanoparticles through the development where metal cations in the host oxide lattice (e.g., perovskite oxides) are exsolved and anchored to the oxide surface under reducing conditions (*8*–*16*).

Although in situ grown nanocatalysts display the advantages of lower cost, higher time efficiency, higher thermal/chemical stability, and enhanced coking resistance compared to catalysts produced by more conventional methods (e.g., wet infiltration or chemical vapor deposition), three major pitfalls have hampered their practical use and commercialization (*17*, *18*): (i) a limited solubility of the exsolving dopant (or catalytic) cations into the host lattice; (ii) many of the dopant cations remain in the bulk, so metal utilization is often low; and (iii) a slow rate of particle generation.

A-site–deficient (A/B <1) perovskites (ABO_3) have been used in an attempt to promote more exsolution of cations to the surface from the bulk by providing a driving force to trigger B-site exsolution (*19*–*21*). However, a limited solubility where only 6 mole percent of the Ti^{4+} was replaced with the cations of interest to be exsolved [e.g., $La_{0.52}Sr_{0.28}Ni_{0.06}Ti_{0.94}O_3$ (*20*)] constrains the number of particles on the surface (*19*, *20*, *22*). Exsolution using voltage-driven reduction (*23*) has been proposed as another strategy to improve the rate of exsolution and increase the population of nanoparticles on the surface; however, it is challenging to use this method for high–surface area materials. Recently, the use of topotactic ion exchange in exsolution (topotactic exsolution) was reported as a new route for promoting a larger number of exsolved cations (*24*). In this case, however, the infiltration technique suffers from the difficulty to control the quantitative amount of catalyst and the need for a large amount of catalyst to wet the parent oxide, thus adding cost with respect to fabrication and materials (*25*).

Therefore, for the ideal use of exsolution, the following requirements must be fulfilled: (i) the production of a larger population of surface particles and (ii) a simple reduction procedure. Within the framework of these criteria, the aim of our work is to meet these requirements by using the topotactic exsolution concept, where Fe guest cations deposited via atomic layer deposition (ALD) can be exchanged with Ni host cations in the A-site–deficient perovskite, $La_{0.6}Sr_{0.2}Ti_{0.85}Ni_{0.15}O_{3-\delta}$. Lanthanum strontium titanates, well-known highly stable catalyst supports, are suitable for this case study with their ability to support a range of A-site deficiency and doping elements. On the basis of the topotactic exsolution that we recently found, a larger number of exsolved particles emerge preferentially on the surface when Fe oxides are externally deposited (*24*). Thus, the deposited Fe guest cation could serve as a general driving force by means of exchanging with the Ni host cation. In this case, the diffusion rate of the deposited guest cation to the host lattice can be an important factor, determining the rate of exsolution through the topotactic ion exchange.

A thin film layer prepared by ALD has been shown to provide a fast diffusion rate with high surface areas and a nanoscale control of the amount of deposition (*26*). As such, ALD renders a uniform, highly quantitative layer of metal oxide at every single step. Therefore, when the Fe guest cation is externally deposited via ALD, the topotactic ion exchange can be accelerated with the help of the fast diffusion rate of the Fe guest cation (*26*), thereby producing a finely

[1]School of Energy and Chemical Engineering, Ulsan National Institute of Science and Technology (UNIST), Ulsan 44919, Republic of Korea. [2]Department of Chemical Engineering, Pohang University of Science and Technology (POSTECH), Pohang 37673, Republic of Korea. [3]UNIST Central Research Facilities and School of Materials Science and Engineering, UNIST, Ulsan 44919, Republic of Korea. [4]Department of Chemical and Biomolecular Engineering, University of Pennsylvania, Philadelphia, PA 19104, USA.
*These authors contributed equally to this work.
†Corresponding author. Email: vohs@seas.upenn.edu (J.M.V.); jwhan@postech.ac.kr (J.W.H.); gtkim@unist.ac.kr (G.K.)

dispersed array of anchored alloy metal nanoparticles with the increased population density. We elucidate the mechanism of the enhanced exsolution via ALD revealed by density functional theory (DFT) calculations. Moreover, the as-exsolved particles exhibit high catalytic activity for the DRM process with no observable degradation in performance for more than 410 hours of continuous operation.

RESULTS

Topotactic exsolution via ALD

In this study, the Ni-doped lanthanum strontium titanate $La_{0.6}Sr_{0.2}Ti_{0.85}Ni_{0.15}O_{3-\delta}$ was selected as a model system to study ALD-modified topotactic exsolution. As in our previous studies of topotactic exsolution, we chose Ni as the exsolving cation because of its higher cosegregation energy compared to other transition metals (e.g., Mn or Fe), and we chose Fe as the guest cation (*27*). The deposition of guest cations was carried out via ALD with varying cycles. The samples after the deposition were reduced at 850°C in a humidified hydrogen atmosphere. Table 1 summarizes the samples that were characterized and the abbreviations we use to denote each composition.

In the original concept of the A-site–deficient perovskite, α moles of A-site vacancies in principle would be able to exsolve up to α moles of metal from the B-site (Eq. 1), creating the stable defect-free ABO_3 stoichiometry with the A/B ratio of unity (ideal case in fig. S1A). However, under typical reducing conditions, only some of the B-site elements can be exsolved, and the inactive cations remain in the bulk, so that the A/B ratio cannot reach unity (step 1 in fig. S1A and Eq. 2). If only the value of the A/B ratio can be lowered, it would lead to a new equilibrium position to make particle exsolution much more dynamic. The topotactic exsolution can be used here as a way to lower the A/B ratio value (*24*). That is, the introduced guest cation B′ can be substituted into the B-site (substitution step in fig. S1B and Eq. 3), enabling the structure to establish a new equilibrium position toward a more active exsolution. As a result, the substitution step could lead to a larger number of exsolved particles. We term this exsolution facilitation process "topotactic exsolution" throughout this study (step 2 in fig. S1B and Eq. 3).

Table 1. Nomenclature for the compounds based on the Fe-deposited LSTN system.

Compound	Abbreviations
$La_{0.6}Sr_{0.2}Ti_{0.85}Ni_{0.15}O_{2.95}$ + reduction	LSTN
$La_{0.6}Sr_{0.2}Ti_{0.85}Ni_{0.15}O_{2.95}$ + 5 cycles of Fe_2O_3 deposition with ALD + reduction	LSTN-5C-Fe
$La_{0.6}Sr_{0.2}Ti_{0.85}Ni_{0.15}O_{2.95}$ + 10 cycles of Fe_2O_3 deposition with ALD + reduction	LSTN-10C-Fe
$La_{0.6}Sr_{0.2}Ti_{0.85}Ni_{0.15}O_{2.95}$ + 15 cycles of Fe_2O_3 deposition with ALD + reduction	LSTN-15C-Fe
$La_{0.6}Sr_{0.2}Ti_{0.85}Ni_{0.15}O_{2.95}$ + 20 cycles of Fe_2O_3 deposition with ALD + reduction	LSTN-20C-Fe
$La_{0.6}Sr_{0.2}Ti_{0.85}Ni_{0.15}O_{2.95}$ + 30 cycles of Fe_2O_3 deposition with ALD + reduction	LSTN-30C-Fe

1 cycle of deposition: exposing to Fe precursor for 360 s followed by oxidation to air.

$$A_{1-\alpha}BO_{3-\delta} \xrightarrow{\text{Exsolution}} (1-\alpha)\,ABO_{3-\delta'} + \alpha B \quad \text{(ideal)} \tag{1}$$

$$A_{1-\alpha}BO_{3-\delta} \xrightarrow{\text{Exsolution:step 1}} A_{1-\alpha}B_{1-\alpha'}O_{3-\delta''} + \alpha' B \quad \text{(conventional exsolution)} \tag{2}$$

$$A_{1-\alpha}BO_{3-\delta} + B'O_{(\text{deposited})} \xrightarrow{\text{Substitution step}} A_{1-\alpha}B_{1-\alpha'}B'_{\beta}O_{3-\delta'''} + \alpha' B \xrightarrow{\text{Topotactic exsolution:step2}} A_{1-\alpha}B_{1-\alpha'-\alpha''}B'_{\beta}O_{3-\delta''''} + (\alpha' + \alpha'')\,B(\text{topotactic exsolution}) \tag{3}$$

The relationship between the ALD cycle and the number of exsolved particles

To provide insight into the topotactic exsolution process, the correlation between the ALD cycle and the number of exsolved particles was investigated using scanning electron microscopy (SEM). Figure 1 (A and B) shows a schematic illustration for the comparison of an existing exsolution and the topotactic exsolution. In the case of the conventional exsolution concept of the A-site–deficient perovskite, a limited fraction of B-site cations can be released toward the incomplete stoichiometry equilibrium under typical reducing conditions. In contrast, for the topotactic exsolution, a larger portion of B-site cations can be pushed out because of the lowered A/B ratio value (fig. S1B). To quantitatively determine the number of exsolved particles in relation to the number of ALD cycles, the number of particles in the corresponding area of the SEM images (Fig. 1, C and D, and fig. S2, C to F) of the reduced pristine and Fe ALD-modified samples was counted by ImageJ software (fig. S2B). As shown in Fig. 1E, the particle population per unit area was found to increase as the number of ALD cycles increases. The average size of particles is shown in Fig. 1F. On the other hand, before reduction, it was confirmed that all samples had a smooth surface regardless of ALD cycles (fig. S2, G and H). The exsolved nanoparticles of 25 to 50 nm are uniformly distributed on the surface of all samples (figs. S2 and S3). It can be seen that the number of ALD cycles does not affect the size of exsolved particles. Notably, at 20 cycles, the particle population reaches 403 particles μm^{-2}, which is about sixfold more than that of pristine $La_{0.6}Sr_{0.2}Ti_{0.85}Ni_{0.15}O_{2.95}$ (LSTN). The number of particles at 30 cycles does not seem to increase, indicating that the facilitation of exsolution is saturated at a certain level of deposition amount. The enhancement in the population density of particles is comparable to that obtained by voltage-driven reduction with a population density of about 400 particles μm^{-2} (*23*).

Furthermore, we confirmed that exsolution is promoted even with a very small amount of ALD-deposited Fe oxide. The growth rate of Fe_2O_3 layer formed by ALD was measured by inductively coupled plasma optical emission spectrometry (ICP-OES), and data are shown in fig. S4. The left axis represents weight % (wt %) of Fe deposited on the LSTN substrate, and the right axis represents moles of Fe for the weight percentage to 1 mol of LSTN. Only 0.011 mol of Fe was required using ALD, whereas 0.176 mol of Fe was necessary using the infiltration method (fig. S4) (*24*). The effectiveness of topotactic exsolution using ALD is about 16 times higher than that using the previous infiltration owing to the features of regular and thin deposition of ALD. Besides, with the advantage of the fast diffusion rate of the Fe oxide layer via ALD, this solution outperforms the existing

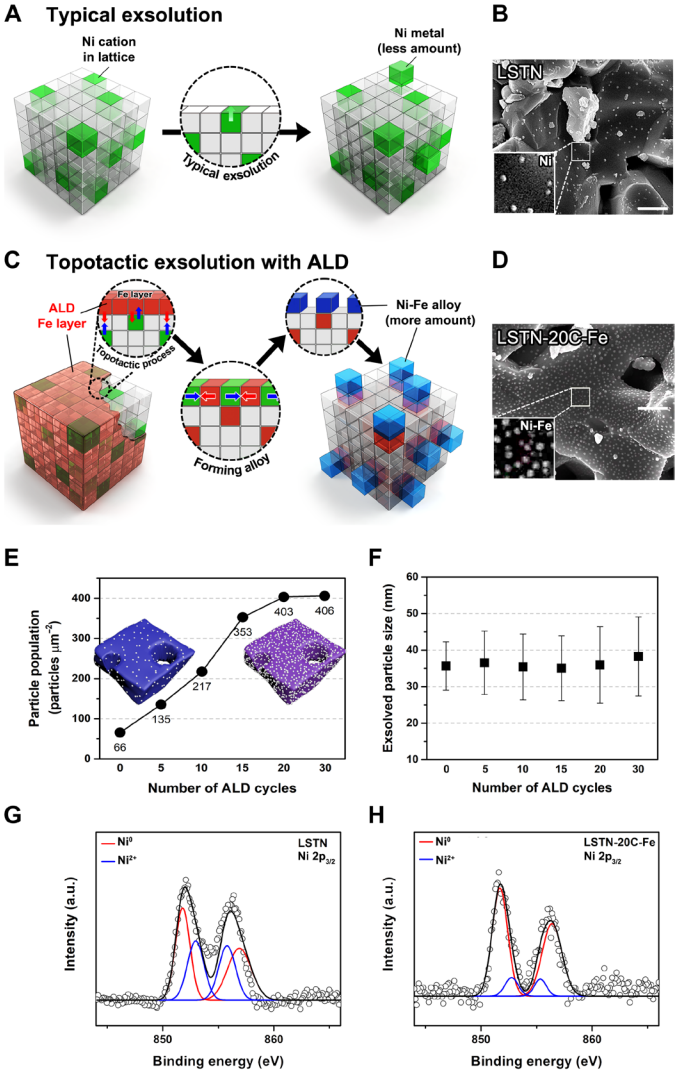

Fig. 1. Schematic comparison, SEM images, the correlation between the number of ALD cycles and the particle size/population, and x-ray photoelectron curves for the samples. (**A**) Conventional exsolution for LSTN and (**B**) corresponding SEM image of LSTN. Scale bar, 500 nm. (**C**) Topotactic exsolution via ALD for LSTN-20C-Fe and the corresponding SEM image of (**D**) LSTN-20C-Fe after reduction. Scale bar, 500 nm. (**E**) Exsolved particle population from 0 to 30 ALD cycles. (**F**) Particle size distribution from 0 to 30 ALD cycles. X-ray photoelectron curves of (**G**) LSTN after reduction and (**H**) LSTN-20C-Fe. a.u., arbitrary units.

methods in terms of the rate of producing nanoparticles. For example, in the case of LSTN-20C-Fe, a similar number of nanoparticles were produced in only 30 min as compared to that of 4 hours of reduction (fig. S5). In comparison, in the sample of LSTN without the deposition of Fe, much fewer particles were formed than LSTN-20C-Fe reduced for 30 min, indicating that topotactic exsolution is advantageous over conventional methods not only quantitatively but also in the length of the process.

X-ray diffraction and x-ray photoelectron spectroscopy

The perovskite oxides were examined by x-ray diffraction (XRD) before and after reduction. In the ABO_3 perovskite structure, the oxygen nonstoichiometry determined by the ratio or type of A/B elements can vary the amount of B-site dopant to be accommodated. We increased the amount of Ni doping by about 2.5 to 5 times compared to that of previous reports (*19*, *20*). Thus, several A-site deficiencies and La^{3+}/Sr^{2+} ratios were attempted to dissolve 0.15 mol Ni as B-site dopant. For example, the A-site and oxygen stoichiometric perovskite with the composition of $La_{0.3}Sr_{0.7}Ti_{0.85}Ni_{0.15}O_3$ displays no secondary phases or NiO peaks in air and even after the reduction, suggesting that Ni exsolution rarely occurs and the composition is not suitable for the exsolution study (fig. S6). The SEM images where the traces of Ni exsolution are hardly seen after a reduction are also in line with the XRD results. For the $La_{0.7}Sr_{0.1}Ti_{0.85}Ni_{0.15}O_3$ A-site deficiency of 0.2 mol with oxygen stoichiometric composition, NiO, La_2O_3, and $SrLa_8Ti_9O_{31}$ were segregated from the perovskite phase, implying that the La-rich composition may destabilize the perovskite structure (fig. S7). Therefore, we reduced a slight amount of La and devised a new composition of LSTN with an A-site deficiency of 0.2 mol. The new composition showed a sufficient solubility of Ni in the B-site without segregation of any secondary structure when sintered at 1200°C in air with pseudocubic lattice parameters of 3.866 Å. Also, as confirmed at around 44.49° (JCPDS card #87-0712) under reducing conditions (fig. S8), Ni exsolution was observed, which is consistent with the SEM results (Fig. 1). After the deposition of Fe oxides through ALD, the patterns of reduced LSTN-20C-Fe do not deviate from those of LSTN in air. This can be interpreted in such a way that the amount of the deposited Fe oxides layer is only a few weight percent (fig. S4) and that it does not affect the XRD pattern (*28*). For the LSTN-20C-Fe as well, the peak for Ni (or Ni-Fe) was observed after a reduction.

X-ray photoelectron spectroscopy (XPS) was conducted to determine the oxidation states of the B-site dopants for the LSTN after reduction and LSTN-20C-Fe. The binding energy peaks of Ni ions are composed of Ni^{2+} $2p_{3/2}$ and Ni metal; 852.96 and 855.78 eV correspond to the peaks of multiplet Ni^{2+} $2p_{3/2}$, and 852.08 and 856.9 eV correspond to the peaks of Ni metal and its satellite feature, respectively. As shown in fig. S8C, the majority of species is NiO without the metallic Ni phase for LSTN in air. In contrast, during the reduction, the splitting of peaks between 850 and 860 eV progresses by the formation of metallic Ni particles due to the exsolution. For the reduced LSTN without the Fe ALD deposition, the metallic phase constitutes about 61% of the total (Fig. 1G). For the LSTN-20C-Fe, this is further intensified, and the ratio of metal was found to be about 87%, which means that most of the Ni in the lattice was exsolved to the surface as a result of the topotactic exsolution. These results are in good agreement with the SEM results, where the number of exsolved particles increases as the number of ALD cycles increases (Fig. 1, C and D, and fig. S2, A to F).

High-resolution transmission electron microscopy analysis

To see the microstructure and composition of the exsolved particles and their interface with the perovskite lattice, we used transmission electron microscopy (TEM). As shown in the high-angle annular dark-field (HAADF) scanning TEM image of LSTN-20C-Fe (Fig. 2A), the nanoparticles with a diameter of around 30 nm were socketed on the surface of the perovskite parent oxide, which is consistent with the previous studies (*20*, *22*). As a result of energy-dispersive spectroscopy (EDS), it is confirmed that the exsolved nanoparticles on the surface are composed of Ni and Fe (Fig. 2B). This is one advantage of the topotactic exsolution bringing about multiple functionalities to the catalysts with producing alloys, as previously

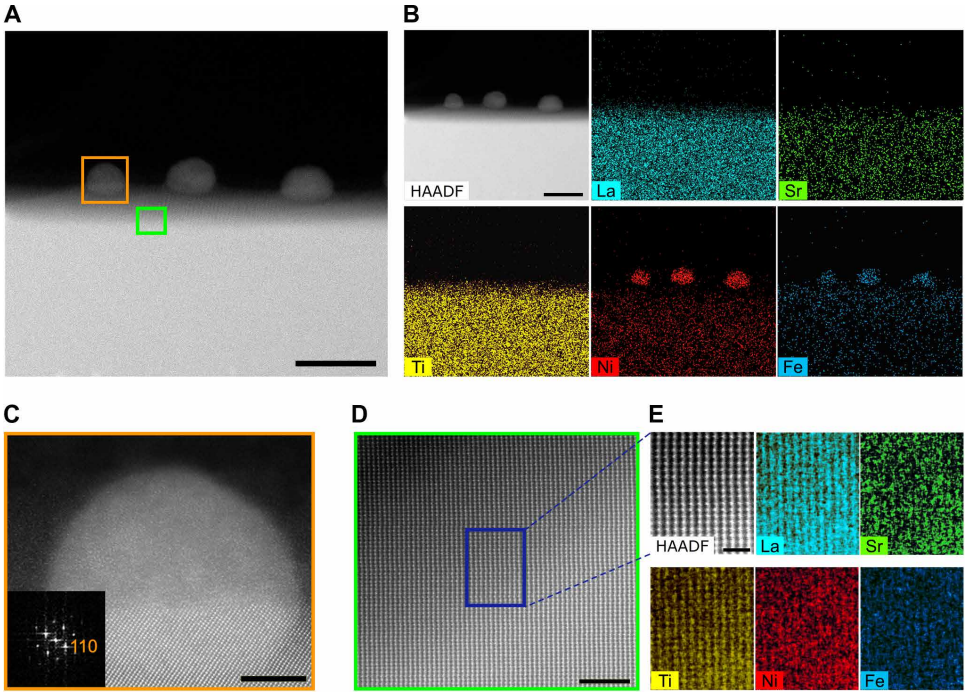

Fig. 2. TEM of exsolved particles on LSTN parent material. (**A**) HAADF scanning TEM image of LSTN-20C-Fe. Scale bar, 40 nm. (**B**) EDS elemental map of La, Sr, Ti, Ni, and Fe. Scale bar, 40 nm. (**C**) HAADF scanning TEM image of LSTN-20C-Fe [orange rectangle in (A)] and the corresponding fast Fourier transformed pattern with zone axis = [100]. Scale bar, 5 nm. (**D**) HAADF scanning TEM image of the enlarged area [green rectangle in (A)]. Scale bar, 3 nm. (**E**) EDS elemental map of La, Sr, Ti, Ni, and Fe in the parent material of LSTN-20C-Fe [blue rectangle in (D)]. Scale bar, 1 nm.

revealed (*24*). As detailed in Table 2, Ni is the major component of the alloy composition at a ratio of 6:4, and Fe also accounts for a considerable amount. This can be explained by the result of DFT calculation, where Fe also tends to exsolve to the surface along with Ni because of its higher cosegregation energy (−1.45 eV) than that of Ti. For the case of the perovskite bulk oxide, the components are identified as La, Sr, Ti, Ni, and Fe (Fig. 2B). The lattice spacing between the planes of the bulk oxide is about 2.78 Å (Fig. 2C), and this value is consistent with the lattice constant of the (110) planes of LSTN-20C-Fe. As shown in Fig. 2 (D and E), the HAADF scanning TEM and detailed atomic-scale scanning EDS mapping were conducted in the parent oxide to confirm the substitution of Fe into the parent LSTN. A pattern of the stripes as displayed in Fig. 2 (D and E) corresponds to the cubic lattice, verifying the presence of the Fe substitution into the lattice.

Table 2. EDS elemental analysis on exsolved Ni-Fe alloy particles on LSTN-10C-Fe and LSTN-20C-Fe.

Exsolved particle	Ni mole ratio of 1 mol Ni-Fe	
Number	LSTN-10C-Fe	LSTN-20C-Fe
Site #1	0.78	0.54
Site #2	0.62	0.66
Site #3	0.65	0.61
Site #4	0.69	0.61
Site #5	0.69	0.64
Site #6	0.70	0.54
Site #7	0.71	0.58
Average	0.69	0.60

DFT calculations

The effect of Fe infiltration on the enhancement of Ni exsolution on LSTN was further elucidated by DFT calculations. On the basis of previous experimental results where B-site metal exsolution preferentially occurred on the (110) termination of LSTN (*20*), we cleaved bulk LST to make LST(110) surface (for the detailed information for modeling LSTN structure, see the Supplementary Materials). We have previously shown that the different cosegregation tendency of transition metal dopants can be used for topotactic exsolution. That is, the cosegregation tendency of the depositing guest ion should be lower than that of the exsolving host ion (*24*, *27*, *29*). Therefore, we examined the cosegregation energies for single dopant elements of various transition metals as well as host Ti cation (Fig. 3A). Our DFT results show that cosegregation energy follows the order of Cu > Ni > Co > Mn > Fe > Cr > Ti (Table 3 and Fig. 3A), implying that Ni in the bulk can be exchanged with deposited Fe. Fe tends to exsolve more easily with higher cosegregation energy than the host Ti of LSTF (Fig. 3B), which agrees with the previous result for Fe exsolution on LSTF (*19*). In addition, DFT-calculated cation exchange energies between guest transition metals and bulk Ni are shown in Fig. 3B. A negative sign in exchange energy indicates that the deposited metal can spontaneously exchange with Ni. Cations of Co, Mn, Fe, Cr, and Ti exhibit spontaneous exchange energy, and the order of the exchange is the opposite of the cosegregation energy. For instance, Fe shows the highest exchange energy of −1.87 eV (Table 3 and Fig. 3, B and C) except for Ti and Cr, which signifies that the surface Fe can be preferentially substituted with the Ni in bulk of

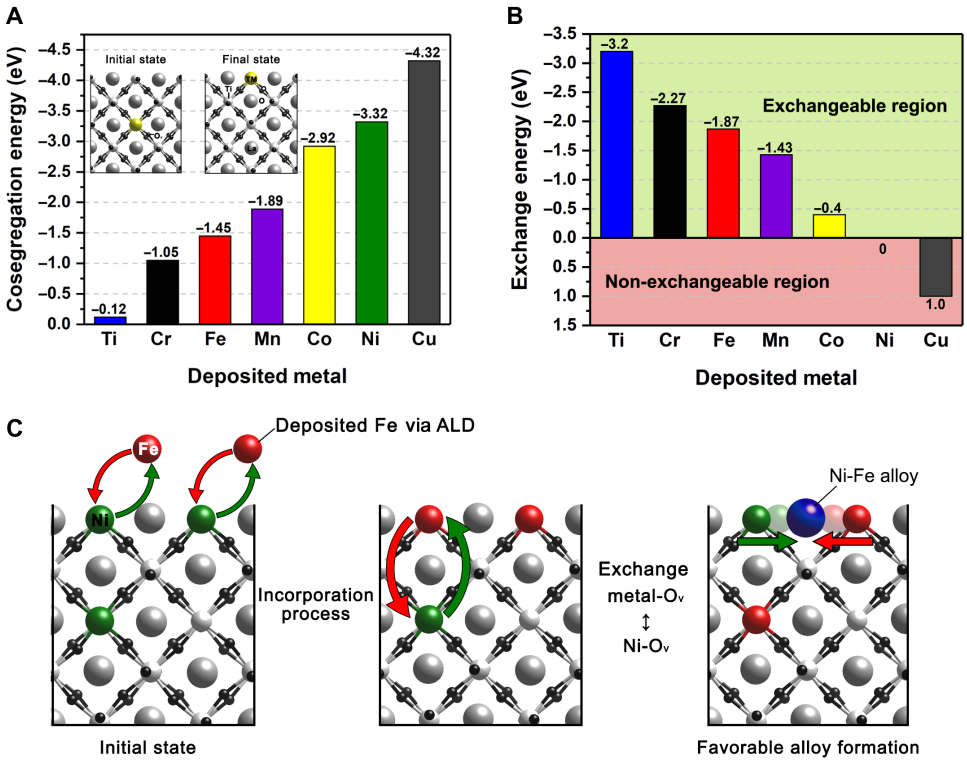

Fig. 3. Schematics of the DFT model for the calculation of B-site metal cosegregation with an oxygen vacancy and cation exchange. (**A**) Cosegregation energy and (**B**) exchange energy comparison of various transition metals. (**C**) Schematics of the DFT calculations of the cation exchange and alloy formation.

Table 3. Cosegregation (B-site metal with an oxygen vacancy) and Ni↔deposited metal exchange energies (in electron volts) on transition metal–doped $La_{0.5}Sr_{0.5}TiO_3$(110).

Bulk	$M\text{-}O_v\text{-}M$ cosegregation energy (eV)	Ni↔TM exchange energy (eV)
Ti	−0.12	−3.20
Cr	−1.05	−2.27
Fe	−1.45	−1.87
Mn	−1.89	−1.43
Co	−2.92	−0.40
Ni	−3.32	0
Cu	−4.32	1.00

LSTN. Contrary to the conventional exsolution where the stoichiometry of the perovskite may reach the limit of stoichiometric equilibrium of A- and B-site cations making the exsolution of Ni sluggish (*20*), for the topotactic exsolution, the deposited Fe on the surface can induce the further exsolution of Ni by exchanging its position with Ni that remained in bulk.

Furthermore, we explored the formation process of Ni-Fe alloy on the LST surface by calculating the surface alloy formation energy based on our previous work (*29*). The formation of Ni-Fe alloy on the LST surface is thermodynamically favorable with the formation energy of −0.43 eV, whereas the alloy formation is not favorable in bulk (0.08 eV). This is in good agreement with the TEM and catalytic property results.

Catalytic property

The catalytic activity of the LSTN-*x*C-Fe for the DRM was evaluated by detecting the exiting gas through the catalyst located in the middle of the fixed-bed tube reactor. Figure 4 compares the catalytic behavior of the LSTN, LSTN-10C-Fe, and LSTN-20C-Fe samples. The catalytic activity was measured in the temperature range of 700° to 900°C with gas hourly space velocity = 30,000 ml g^{-1} $hour^{-1}$. As depicted in Fig. 4A, the reacted methane for the LSTN-10C-Fe is slightly improved compared to LSTN, but that for the LSTN-20C-Fe is remarkably improved at 64% compared to that of LSTN. In particular, as the temperature decreases, the degree of the activity decline is inversely proportional to the number of ALD cycles, which is related to the activation energy shown in Fig. 4B. The activation energies of LSTN and LSTN-10C-Fe are similar, and it decreases greatly at LSTN-20C-Fe, so it is presumed that the reactivity of the catalysts is proportional either to the number of exsolved particles or to the degree of the alloy formation. To identify this presumption, the three different ratios of Ni-Fe alloy catalysts [e.g., the ratios of Ni to Fe are 1.0 to 0 (bulk Ni), 0.70 to 0.30 (bulk Ni-Fe 0.70), and 0.60 to 0.40 (bulk Ni-Fe 0.60), respectively] on an inert support γ-Al_2O_3 were evaluated for the DRM test. In this way, the mechanism of the DRM can be assessed with a monofunctional pathway, where the methane reactant is dependent on the metal alone. As depicted in Fig. 4 (C and D), Arrhenius-type plots for bulk Ni and bulk Ni-Fe alloys were plotted, from which the activation energies were calculated. The trends of the activation energy for the alloy catalysts on inert support appear analogous to those for the LSTN series, which demonstrates that the different ratios of Ni-Fe alloys were formed depending on the number of ALD cycles. This is supported by EDS elemental analysis shown in Table 2, e.g., the average

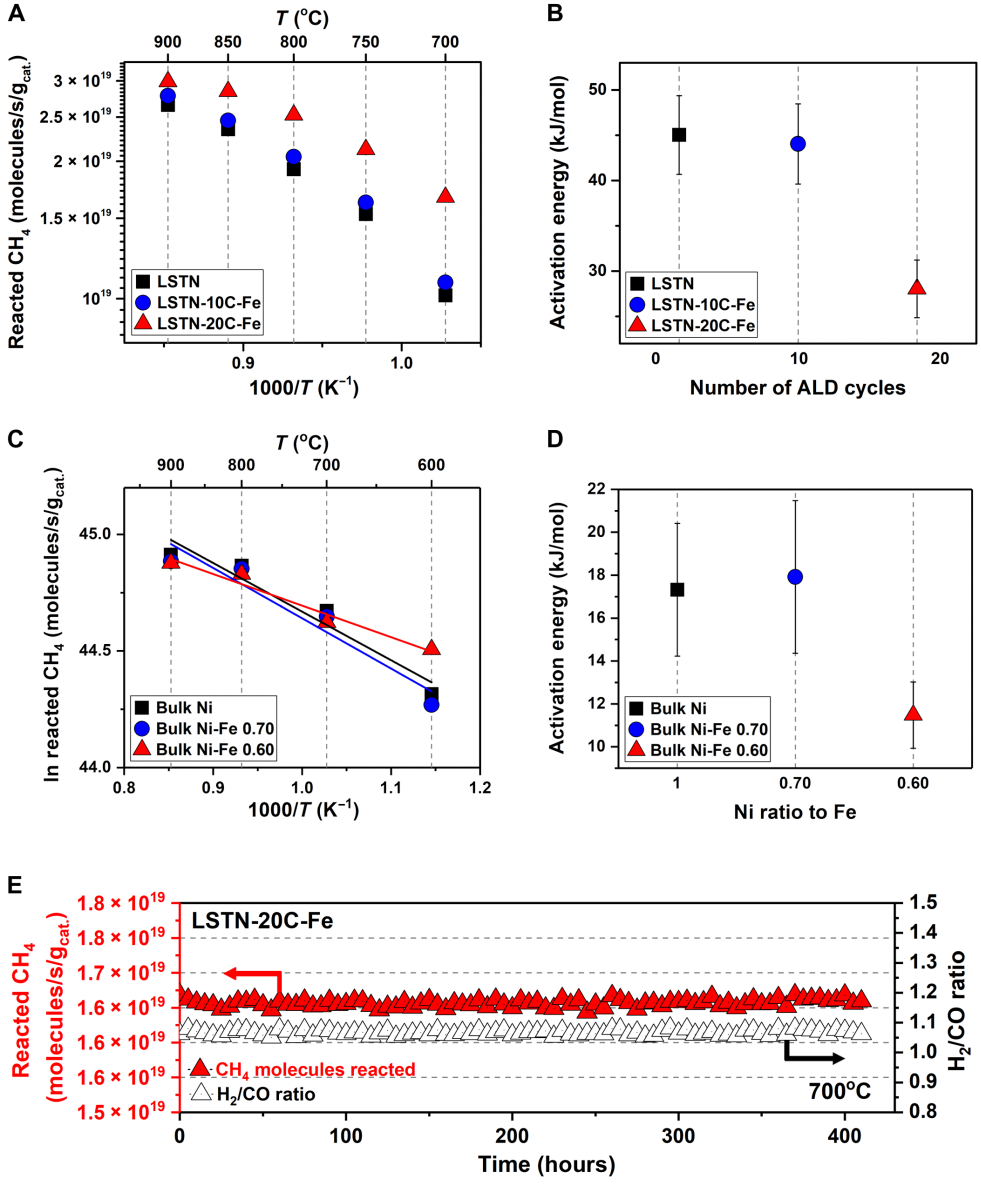

Fig. 4. Catalytic properties for the DRM. (**A**) Reacted methane during the DRM reaction for LSTN, LSTN-10C-Fe, and LSTN-20C-Fe. (**B**) The activation energy of the methane reactivity calculated for LSTN, LSTN-10C-Fe, and LSTN-20C-Fe. (**C**) Arrhenius-type plots of reacted CH_4 for bulk Ni and bulk Ni-Fe alloy catalysts. (**D**) The activation energy of the methane reactivity calculated for bulk Ni, bulk Ni-Fe 0.70, and bulk Ni-Fe 0.60. (**E**) Time dependence of CH_4 reactivity and H_2/CO ratio for LSTN-20C-Fe in DRM at 700°C.

ratio of Ni to Fe is around 0.60 to 0.40 for the LSTN-20C-Fe sample. According to the DFT results, Fe also has a higher alloy formation energy, which is in accordance with the experimental result where the more Fe cations are substituted into the bulk, the higher is the ratio of Fe in Ni-Fe alloy. In addition, the stability of the particles obtained via topotactic exsolution was evaluated for LSTN-20C-Fe. In continuous DRM measurements (Fig. 4E), the CH_4 reactivity remained constant over 400 hours, validating the durability of the supported metal catalyst.

DISCUSSION

In conclusion, we have used topotactic exsolution reinforced by ALD on the widely used perovskite oxide, nickel-doped lanthanum strontium titanate. As an effective means of producing alloy nanoparticles, topotactic exsolution with ALD has several noteworthy implications, including (i) a larger population of exsolved nanoparticles, (ii) the selective formation of alloy catalysts, and (iii) a faster rate of nanoparticle generation. Fe as guest transition metal exhibits an exchange energy of −1.87 eV with host Ni, resulting in the spontaneous exchange between Ni and Fe topotactic exsolution. The bimetallic catalysts spontaneously produced in a short time are also excellent in catalytic activity in DRM, which not only improved the initial value by 64% compared to pristine LSTN but also reduced the activation energy by about 40% with a prolonged stability of 410 hours. This newly developed topotactic exsolution with ALD could serve as a general driving force applicable to other exsolution systems.

MATERIALS AND METHODS

Synthesis of perovskite materials

All samples of the perovskite structure were synthesized by the Pechini sol-gel method (*30*–*32*). Adequate amounts of $La(NO_3)_3.6H_2O$, $Sr(NO_3)_2$, and $Ni(NO_3)_2.6H_2O$ for stoichiometry were dissolved in distilled water. An adequate amount of $Ti[OCH(CH_3)_2]_4$ was dissolved in ethanol separately for ionization, and then ethylene glycol/citric acid as complexing agents were added to this solution. All solutions were mixed together and stirred overnight. A combustion process above 300°C on a heating plate is followed to obtain fine powders. The powders were calcined at 600°C for 4 hours to remove residual organics. The synthesized powders and their abbreviations are given in Table 1.

ALD of Fe oxide film

The iron oxide films on LSTN were prepared by ALD using a home-built apparatus. A picture of the apparatus is shown in fig. S10. The apparatus consists of quartz chambers containing precursor/substrate, dosing lines, and valves connecting the chambers. Each chamber was enclosed by individual ovens to allow separate temperature control. Also, a mechanical vacuum pump was used to evacuate the chambers at approximately 10^{-3} torr (*26*, *33*).

The condition used for depositing the precursor ferrocene [$Fe(Cp)_2$; Sigma-Aldrich] was adopted from a previous publication (*28*). After evacuating the $Fe(Cp)_2$ precursor chamber at room temperature, it was heated to 160°C to produce a reasonable vapor pressure of $Fe(Cp)_2$. During the deposition cycles, the $Fe(Cp)_2$ vapor was introduced to the evacuated substrate chamber, which contained approximately 0.2 g of LSTN. The LSTN substrate was exposed to the vapor of $Fe(Cp)_2$ multiple times at 350°C for 360 s to confirm that the reaction with the surface was complete. Excess precursor in the substrate chamber was then removed by evacuation, and the substrate was oxidized by exposing it to air for 300 s.

Exsolution characterization

To compare the number of exsolution particles varying with the cycles of Fe oxide deposition via ALD, LSTN and other perovskite oxides were sintered at 1200°C as substrates. After the deposition through ALD, all samples were reduced at 850°C for 4 hours in H_2 atmosphere (with 3% H_2O).

The elemental analysis of the LSTN-*x*C-Fe samples (x = 0, 5, 10, 15, 20, and 30) for individual elements was quantified by ICP-OES. In the measurement, a Spectro Genesis spectrometer was used in conjunction with a concentric nebulizer. For the ICP-OES process, all samples for analysis (~50 mg) were dissolved in a 16-ml solution of Aqua Regia for 4 hours at 200°C. Then, the solution was distilled with a 5 wt % HNO_3 solution to attain the appropriate concentration for the ICP analysis.

The crystal structures of samples were analyzed by XRD (Bruker D8 Advance, Cu Kα radiation, 40 kV, 40 mA). The surface morphologies of the material were observed through SEM (FEI Nova Nano 230 FE-SEM). The number of particles on the oxide surface was evaluated by ImageJ software. In the selected SEM images with appropriate magnification, the contrast and sharpness were slightly adjusted. The adjusted image was outlined based on the contrast to count the number of particles and to calculate the size of the particles (fig. S2B). XPS analysis was performed using ESCALAB 250XI from Thermo Fisher Scientific with a monochromatic A1-Ka (ultraviolet He1, He2) x-ray source. Cross-sectional samples for the TEM analysis were prepared by using a focused ion beam (FIB; Helios 450HP, FEI). TEM images were obtained with a FEI Titan 3 G2 60-300 with an image-forming Cs corrector at an accelerating voltage of 80 kV.

Density functional theory

DFT calculations were performed using the Vienna Ab initio Simulation Package (*34*, *35*). Exchange-correlation energies were treated by the Perdew-Burke-Ernzerhof functional based on generalized gradient approximation (GGA) (*36*). A plane-wave expansion with a cutoff of 400 eV was used with a 4 × 2 × 1 Monkhorst-Pack k-point sampling of the Brillouin zone for all slab model calculations (*37*). Gaussian smearing was used with a width of 0.05 eV to determine partial occupancies. Geometries were relaxed using a conjugate gradient algorithm until the forces on all unconstrained atoms were less than 0.03 eV/Å. To take into account on-site Coulomb and exchange interactions, we used GGA + U schemes with effective U values of 4.36, 4.0, and 6.0 for Ti, Fe, and Ni, respectively (*27*). On the basis of our experimental observation, we constructed the pseudocubic $La_{0.5}Sr_{0.5}TiO_3$ with $a = b = c = 7.910$. Among the two possible cation configurations, we used a more stable configuration (fig. S9), which had a lower total energy of 0.19 eV.

To examine the segregation tendency of dopant elements, we constructed surface models by cleaving the DFT-optimized LST bulk along the (110) direction, which has been reported as the most preferred facet of B-site metal exsolution on $La_{0.5}Sr_{0.5}TiO_{3-\delta}$-based perovskites (fig. S9, E and F). A nine-layered LST slab was used with a vacuum thickness of up to 17 Å (fig. S9). The cosegregation energy of B-site metal (E_{seg}) with an oxygen vacancy is defined as below (*27*)

$$E_{co-seg} = E_{(B-Vo)surf} - E_{(B-Vo)bulk}$$

where $E_{(B-Vo)surf}$ and $E_{(B-Vo)bulk}$ are the total energies of the system with the B-site metal located at the surface and in the bulk with an oxygen vacancy, respectively. By our definition, more negative energy indicates easier exsolution.

Catalytic activity

The catalytic activity of the catalysts was assessed with a fixed-bed quartz tube reactor with an internal diameter of about 10 mm. Approximately 0.2 g of sample powder was placed in the middle of the reactor. For the DRM test, the sample powder was reduced in situ in H_2 atmosphere (with 3% H_2O) at 900°C for 1 hour. After the reduction, the remaining H_2 gas was purged with dry He, and then the gas mixture of CO_2, CH_4, and He was introduced to the reactor with a ratio of 10:10:80 ml min^{-1}, respectively. Compositional analysis of the effluent gases from the reaction was performed using gas chromatography (GC) (Agilent 7820A GC instrument) with a thermal conductivity detector and a packed column (Agilent Carboxen 1000). The gas flow was measured using a mass flow controller (Atovac GMC1200) and calibrated through a bubble flow meter for a more accurate ratio calculation. The DRM reaction is shown below, and the CH_4 reactivity and CH_4 conversion were obtained from the following equation

$$CH_4 + CO_2 \leftrightarrow 2CO + 2H_2 \ (\Delta H^0_{298K} = 247 \text{ kJ/mol})$$

$$CH_4 \text{ reactivity } \left[\frac{\text{molecules}}{\text{s} \cdot \text{g}_{\text{cat.}}}\right] = \frac{H_{2detect}\,[\text{molecules/s}]}{2 \times \text{weight of catalyst [g]}}$$

$$\mathrm{CH_4\ conversion} = \frac{[\mathrm{CH_4}]_{\mathrm{consumed}}}{[\mathrm{CH_4}]_{\mathrm{feed}}} \times 100\,\% = \frac{[\mathrm{H_2}]_{\mathrm{detect}}}{[\mathrm{H_2}]_{\mathrm{detect}} + 2\,[\mathrm{CH_4}]_{\mathrm{detect}}} \times 100\%$$

The Arrhenius equation is given by the following equation

$$k = A\,e^{-E_a/(RT)}$$

where A is the pre-exponential factor for the reaction, R is the universal gas constant, T is the absolute temperature (in kelvin), and k is the reaction rate coefficient. Taking the logarithm to the Arrhenius equation, the activation energy (E_a) can be evaluated from the slopes of the lines. The values of slopes were obtained from fitting values in a graph of a function of temperature.

SUPPLEMENTARY MATERIALS

Supplementary material for this article is available at http://advances.sciencemag.org/cgi/content/full/6/35/eabb1573/DC1

REFERENCES AND NOTES

1. D. Pakhare, J. Spivey, A review of dry (CO_2) reforming of methane over noble metal catalysts. *Chem. Soc. Rev.* **43**, 7813–7837 (2014).
2. P. I. Cowin, C. T. G. Petit, R. Lan, J. T. S. Irvine, S. Tao, Recent progress in the development of anode materials for solid oxide fuel cells. *Adv. Energy Mater.* **1**, 314–332 (2011).
3. S. Sengodan, S. Choi, A. Jun, T. H. Shin, Y.-W. Ju, H. Y. Jeong, J. Shin, J. T. S. Irvine, G. Kim, Layered oxygen-deficient double perovskite as an efficient and stable anode for direct hydrocarbon solid oxide fuel cells. *Nat. Mater.* **14**, 205–209 (2015).
4. P. Szuromi, Watching metal nanoparticle exsolution. *Science* **366**, 834–835 (2019).
5. J. Lu, C. Zhu, C. Pan, W. Lin, J. P. Lemmon, F. Chen, Highly efficient electrochemical reforming of CH_4/CO_2 in a solid oxide electrolyser. *Sci. Adv.* **4**, eaar5100 (2018).
6. V. Kyriakou, D. Neagu, G. Zafeiropoulos, R. K. Sharma, C. Tang, K. Kousi, I. S. Metcalfe, M. C. M. van de Sanden, M. N. Tsampas, Symmetrical exsolution of Rh nanoparticles in solid oxide cells for efficient syngas production from greenhouse gases. *ACS Catal.* **10**, 1278–1288 (2020).
7. Y. Chen, S. Yoo, K. Pei, D. Chen, L. Zhang, R. Murphy, B. Zhao, Y. Zhang, Y. Chen, M. Liu, An in situ formed, dual-phase cathode with a highly active catalyst coating for protonic ceramic fuel cells. *Adv. Funct. Mater.* **28**, 1704907 (2018).
8. Y. Nishihata, J. Mizuki, T. Akao, H. Tanaka, M. Uenishi, M. Kimura, T. Okamoto, N. Hamada, Self-regeneration of a Pd-perovskite catalyst for automotive emissions control. *Nature* **418**, 164–167 (2002).
9. R. Shiozaki, A. G. Andersen, T. Hayakawa, S. Hamakawa, K. Suzuki, M. Shimizu, K. Takehira, Partial oxidation of methane over a Ni/$BaTiO_3$ catalyst prepared by solid phase crystallization. *J. Chem. Soc. Faraday Trans.* **93**, 3235–3242 (1997).
10. Y. Gao, D. Chen, M. Saccoccio, Z. Lu, F. Ciucci, from material design to mechanism study: Nanoscale Ni exsolution on a highly active A-site deficient anode material for solid oxide fuel cells. *Nano Energy* **27**, 499–508 (2016).
11. Y. Li, W. Zhang, Y. Zheng, J. Chen, B. Yu, Y. Chen, M. Liu, Controlling cation segregation in perovskite-based electrodes for high electro-catalytic activity and durability. *Chem. Soc. Rev.* **46**, 6345–6378 (2017).
12. G. Dimitrakopoulos, A. F. Ghoniem, B. Yildiz, In situ catalyst exsolution on perovskite oxides for the production of CO and synthesis gas in ceramic membrane reactors. *Sustain. Energy Fuels* **3**, 2347–2355 (2019).
13. N. W. Kwak, S. J. Jeong, H. Gil Seo, S. Lee, Y. Kim, J. K. Kim, P. Byeon, S.-Y. Chung, W. Jung, In situ synthesis of supported metal nanocatalysts through heterogeneous doping. *Nat. Commun.* **9**, 4829 (2018).
14. Y.-R. Jo, B. Koo, M.-J. Seo, J. K. Kim, S. Lee, K. Kim, J. W. Han, W. C. Jung, B.-J. Kim, Growth kinetics of individual co particles ex-solved on $SrTi_{0.75}Co_{0.25}O_{3-\delta}$ polycrystalline perovskite thin films. *J. Am. Chem. Soc.* **141**, 6690–6697 (2019).
15. X. Lv, H. Chen, W. Zhou, F. Cheng, S.-D. Li, Z. Shao, Direct-methane solid oxide fuel cells with an in situ formed Ni–Fe alloy composite catalyst layer over Ni–YSZ anodes. *Renew. Energy* **150**, 334–341 (2020).
16. K. Kousi, D. Neagu, L. Bekris, E. I. Papaioannou, I. S. Metcalfe, Endogenous nanoparticles strain perovskite host lattice providing oxygen capacity and driving oxygen exchange and CH_4 conversion to syngas. *Angew. Chemie. Int. Ed.* **59**, 2510–2519 (2020).
17. H. Han, J. Park, S. Y. Nam, K. J. Kim, G. M. Choi, S. S. P. Parkin, H. M. Jang, J. T. S. Irvine, Lattice strain-enhanced exsolution of nanoparticles in thin films. *Nat. Commun.* **10**, 1471 (2019).
18. M. B. Katz, S. Zhang, Y. Duan, H. Wang, M. Fang, K. Zhang, B. Li, G. W. Graham, X. Pan, Reversible precipitation/dissolution of precious-metal clusters in perovskite-based catalyst materials: Bulk versus surface re-dispersion. *J. Catal.* **293**, 145–148 (2012).
19. D. Neagu, G. Tsekouras, D. N. Miller, H. Ménard, J. T. S. Irvine, In situ growth of nanoparticles through control of non-stoichiometry. *Nat. Chem.* **5**, 916–923 (2013).
20. D. Neagu, T.-S. Oh, D. N. Miller, H. Ménard, S. M. Bukhari, S. R. Gamble, R. J. Gorte, J. M. Vohs, J. T. S. Irvine, Nano-socketed nickel particles with enhanced coking resistance grown in situ by redox exsolution. *Nat. Commun.* **6**, 8120 (2015).
21. Y. Zhu, X. Liu, S. Jin, H. Chen, W. Lee, M. Liu, Y. Chen, Anionic defect engineering of transition metal oxides for oxygen reduction and evolution reactions. *J. Mater. Chem. A* **7**, 5875–5897 (2019).
22. T.-S. Oh, E. K. Rahani, D. Neagu, J. T. S. Irvine, V. B. Shenoy, R. J. Gorte, J. M. Vohs, Evidence and model for strain-driven release of metal nanocatalysts from perovskites during exsolution. *J. Phys. Chem. Lett.* **6**, 5106–5110 (2015).
23. J.-h. Myung, D. Neagu, D. N. Miller, J. T. S. Irvine, Switching on electrocatalytic activity in solid oxide cells. *Nature* **537**, 528–531 (2016).
24. S. Joo, O. Kwon, K. Kim, S. Kim, H. Kim, J. Shin, H. Y. Jeong, S. Sengodan, J. W. Han, G. Kim, Cation-swapped homogeneous nanoparticles in perovskite oxides for high power density. *Nat. Commun.* **10**, 697 (2019).
25. D. Ding, X. Li, S. Y. Lai, K. Gerdes, M. Liu, Enhancing SOFC cathode performance by surface modification through infiltration. *Energ. Environ. Sci.* **7**, 552–575 (2014).
26. C. Lin, J. B. Jang, L. Zhang, E. A. Stach, R. J. Gorte, Improved coking resistance of "intelligent" Ni catalysts prepared by atomic layer deposition. *ACS Catal.* **8**, 7679–7687 (2018).
27. O. Kwon, S. Sengodan, K. Kim, G. Kim, H. Y. Jeong, J. Shin, Y.-W. Ju, J. W. Han, G. Kim, Exsolution trends and co-segregation aspects of self-grown catalyst nanoparticles in perovskites. *Nat. Commun.* **8**, 15967 (2017).
28. T. M. Onn, M. Monai, S. Dai, E. Fonda, T. Montini, X. Pan, G. W. Graham, P. Fornasiero, R. J. Gorte, Smart Pd catalyst with improved thermal stability supported on high-surface-area $LaFeO_3$ prepared by atomic layer deposition. *J. Am. Chem. Soc.* **140**, 4841–4848 (2018).
29. O. Kwon, K. Kim, S. Joo, H. Y. Jeong, J. Shin, J. W. Han, S. Sengodan, G. Kim, Self-assembled alloy nanoparticles in layered double perovskite as a fuel oxidation catalyst for solid oxide fuel cells. *J. Mater. Chem. A* **6**, 15947–15953 (2018).
30. D. Chen, R. Ran, K. Zhang, J. Wang, Z. Shao, Intermediate-temperature electrochemical performance of a polycrystalline $PrBaCo_2O_{5+\delta}$ cathode on samarium-doped ceria electrolyte. *J. Power Sources* **188**, 96–105 (2009).
31. Z. Shao, W. Yang, Y. Cong, H. Dong, J. Tong, G. Xiong, Investigation of the permeation behavior and stability of a $Ba_{0.5}Sr_{0.5}Co_{0.8}Fe_{0.2}O_{(3-\delta)}$ oxygen membrane. *J. Memb. Sci.* **172**, 177–188 (2000).
32. G. Chen, W. Zhou, D. Guan, J. Sunarso, Y. Zhu, X. Hu, W. Zhang, Z. Shao, Two orders of magnitude enhancement in oxygen evolution reactivity on amorphous $Ba_{0.5}Sr_{0.5}Co_{0.8}Fe_{0.2}O_{3-\delta}$ nanofilms with tunable oxidation state. *Sci. Adv.* **3**, e1603206 (2017).
33. C. Lin, A. C. Foucher, Y. Ji, C. D. Curran, E. A. Stach, S. McIntosh, R. J. Gorte, "Intelligent" Pt catalysts studied on high-surface-area $CaTiO_3$ films. *ACS Catal.* **9**, 7318–7327 (2019).
34. G. Kresse, J. Furthmüller, Efficient iterative schemes for ab initio total-energy calculations using a plane-wave basis set. *Phys. Rev. B* **54**, 11169–11186 (1996).
35. G. Kresse, J. Hafner, Norm-conserving and ultrasoft pseudopotentials for first-row and transition elements. *J. Phys. Condens. Matter* **6**, 8245–8257 (1994).
36. J. P. Perdew, K. Burke, M. Ernzerhof, Generalized gradient approximation made simple. *Phys. Rev. Lett.* **77**, 3865–3868 (1996).
37. H. J. Monkhorst, J. D. Pack, Special points for Brillonin-zone integrations. *Phys. Rev. B* **13**, 5188–5192 (1976).

Acknowledgments

Funding: This work was supported by the Korea Institute of Energy Technology Evaluation and Planning (KETEP); the Ministry of Trade, Industry and Energy (MOTIE) of the Republic of Korea (no. 20173020032120); and the Mid-Career Researcher Program (NRF-2018R1A2A1A05077532) through the National Research Foundation (NRF) of Korea, funded by the Ministry of Science, ICT, and Future Planning. This work was also supported by the Global Ph.D. Fellowship Program through an NRF Grant funded by the Korean Government (NRF-2018H1A2A1060644). **Author contributions:** S.J. conceived the experiments and wrote the manuscript. A.S. contributed to layer deposition via ALD and designing schematics. O.K. and J.H.L. performed TEM analysis. K.K. and J.W.H. performed the DFT calculations. R.J.G. and J.M.V. gave constructive comments. All the authors contributed to the discussions and analysis of the results regarding the manuscript. G.K. directed the team. **Competing interests:** The authors declare that they have no competing interests. **Data and materials availability:** All data needed to evaluate the conclusions in the paper are present in the paper and/or the Supplementary Materials. Additional data related to this paper may be requested from the authors.

Submitted 24 February 2020
Accepted 10 July 2020
Published 26 August 2020
10.1126/sciadv.abb1573

Citation: S. Joo, A. Seong, O. Kwon, K. Kim, J. H. Lee, R. J. Gorte, J. M. Vohs, J. W. Han, G. Kim, Highly active dry methane reforming catalysts with boosted in situ grown Ni-Fe nanoparticles on perovskite via atomic layer deposition. *Sci. Adv.* **6**, eabb1573 (2020).